Journal of Alloys and Compounds 817 (2020) 152735

Contents lists available at ScienceDirect

Journal of Alloys and Compounds

journal homepage: http://www.elsevier.com/locate/jalcom

Assessing the solid-state kinetics and behavior for uranium-free Pu-12Am–40Zr alloys at 973 K

Jeffery A. Aguiar [a, *], Brandon D. Miller [a], Yasushi Tsuboi [b], Thomas Johnson [a], Kazuo Arie [b], Robert D. Mariani [a]

[a] Idaho National Laboratory, 2525, Fremont Ave., Idaho Falls, ID, USA
[b] Toshiba Energy Systems and Solutions Corporation, Japan

ARTICLE INFO

Article history:
Received 8 June 2019
Received in revised form
15 October 2019
Accepted 19 October 2019
Available online 23 October 2019

Keywords:
Uranium-free Pu-based fuels
Solid state kinetics
Solid state chemistry
Transmission electron microscopy
Gen IV nuclear reactors

ABSTRACT

Uranium-free nonfertile Pu-based alloys, including Pu–40Zr and Pu-12Am–40Zr, represent two candidate fuel alloys for Generation IV (GEN-IV) and transuranic (TRU) type burner reactors. Before their acceptance in these applications, the chemical compatibility and interaction layer growth between these alloys and suggested HT-9 cladding must be reported in detail to facilitate their acceptance in advanced reactor concepts. In this study, each alloy was studied at 700 °C (973 K) for a variable period of time between 100 and 200 h in a diffusion couple geometry with Cr and V. Comparing the 100–200 h tests between Pu-12Am–40Zr fuel and Cr with V suggests a weakening in the interfacial growth rate as a function of annealing time. A quantitative study on the solid-state behavior and evolution of Pu-Am-Zr interacting with both Cr and V barriers at 700 °C (973 K) is reported.

1. Introduction

Closing the nuclear fuel cycle is a major global technical challenge to the acceptance and expansion of current and advanced nuclear technology around the world [1]. The Generation IV (GEN-IV) program and the Global Nuclear Energy Partnership (GNEP) have adopted goals to minimize long-lived transuranics (TRUs) stored in high-level waste repositories and mitigate proliferation risks [1,2]. In the case that TRUs are burned in fast reactors, the radiotoxicity and heat load of nuclear wastes can be reduced close to levels of natural uranium after approximately hundreds of years, instead of tens of thousands of years or longer [3]. The burning of TRU-bearing fuels—mainly Pu, Np, and Am bearing—in advanced GEN-IV fast reactors is therefore recognized as one approach that will at least minimize the heat load and footprint of nuclear waste repositories and reduce proliferation concerns.

Uranium-free fuels are recognized as the most attractive because the absence of ^{238}U renders the fuel non-fertile; that is additional ^{239}Pu is not generated through the process of neutron-activation of ^{238}U followed by double-beta decay to ^{239}Pu. Two particular non-fertile fuel alloys have been irradiated: Pu-12Am–40Zr and Pu–40Zr (values in weight percent, wt%, see Table 1). Their irradiation history has suggested further study using out-of-pile materials compatibility tests, specifically with potential barrier layers between the fuel alloy (fuel meat) and cladding [4]. Plutonium is known to form a low-temperature eutectic with iron, and since fast-reactor cladding materials commonly contain iron, an enhanced safety margin is introduced through the careful selection of barrier layer.

Due to high temperatures, physicochemical gradients arising from fission products, phase formation, and a high number of atomic displacements, fast nuclear reactors present extreme materials challenges. [5]. The Experimental Breeder Reactor II (EBR-II) established some benchmarks for metallic fast reactor fuel driver fuel, with a focus on U–10Zr and U-Pu-10Zr fuels [6–9]. Zirconium raises the solidus of the metallic fuel sufficiently to enhance the melting temperature safety margin, while additions of plutonium depress the solidus and affect the fuel melting temperature. A compositional balance between zirconium and plutonium is required to preserve not only the melt-casting system and operational ease of the fuel slug fabrication, but maintain a significant safety margin with respect to fuel melting. Previous studies suggest the fuel composition of a uranium-free system should contain

* Corresponding author.
E-mail addresses: Jeffery.Aguiar@inl.gov (J.A. Aguiar), Brandon.Miller@inl.gov (B.D. Miller), thomas.johnson@inl.gov (T. Johnson), robert.mariani@inl.gov (R.D. Mariani).

https://doi.org/10.1016/j.jallcom.2019.152735
0925-8388/

Table 1
Diffusion couple materials and experimental parameters.

Diffusion Couple Name	Diffusion Couple Materials			Experimental Properties	
	Fuel Type	Barrier 1	Barrier 2	Temperature (°C)	Duration (hours)
DC1	Pu–40Zr	V	Annealed Cr	700	100
DC2	Pu-12Am–40Zr	V	Annealed Cr	700	100
DC3	Pu-12Am–40Zr	As-received Cr	Annealed Cr	700	200

approximately 30–40 wt% zirconium to accommodate these same competing concerns for fuel safety margins and ease of fabrication. Phase relations in the uranium free quaternary plutonium–americium–zirconium (Pu–Am-Zr) alloys have not yet been extensively reported [8]. At concentrations below 10 wt%, zirconium does not raise the liquidus to challenge ease of fabrication and hence has been used.

Within the community concerns have now shifted to reporting on fuel-cladding chemical interactions (FCCI) that have not been studied for these compositions [10,11]. Initial out-of-pile annealing tests with diffusion couples reported the initial findings for U-10Zr and U-Pu-10Zr fuels with chromium (Cr) and vandadium (V) barrier materials suggested a more complex behavior requiring further analysis [12]. This report provides a more in-depth study into the interaction between these two fuel alloys with Cr and V barriers with regard to annealing time.

Here we report out-of-pile compatibility studies with these two fuel alloys using Cr and V as barrier materials between the fuel meat and barrier material. In particular, the solid-state kinetics and chemical interaction between Pu–40Zr and Pu-12Am–40Zr are studied for two durations, 100 and 200 h, at 973 K. The reaction mechanisms were analyzed using SEM and TEM. The TEM studies revealed intercalations at the interfaces with both Pu–40Zr and Pu-12Am–40Zr, indicating a reaction front rendered sluggish in the 200 h anneal. The principal factors contributing to the qualitatively good performance of these alloys appear to be their solid-state kinetics and evolved microstructures at their fuel-barrier interfaces.

2. Experimental setup and characterization techniques

2.1. Experimental setup

We selected two U free-Pu alloys with nominal compositions of Pu–40Zr and Pu-12Am–40Zr (in wt%) for this diffusion couple experiment. In each experiment, the fuel was arc cast in an inert atmosphere glove box with a drop casting technique. The produced cylindrical fuel slugs were sectioned into several pieces designated for assembling a diffusion couple. Chromium (Cr) and Vanadium (V) cladding material with 99.98% purity and 0.02% max metal impurity level were obtained from Alfa Aesar. Three different diffusion couples utilizing Pu–Zr based fuels were fabricated to understand Cr and V barrier effectiveness in reducing the interaction layer growth between the Pu–Zr based fuels and the HT-9 cladding. The three diffusion couple experimental setups and parameters are listed in Ishii et al. [11]. The diffusion couple materials and properties were chosen to focus on the effect of different diffusion barriers, annealing time, and fuel alloy composition on the formation and kinetics associated with the interaction layer between the fuel and cladding.

Each of the materials used in building the three diffusion couples went through a similar preparation process to be sized and polished for testing. Each material was prepared in an air atmosphere. The HT-9 steel was machined from rod stock to a diameter of 5 mm and sectioned into disks up to 3 mm thick. The HT-9 surfaces were polished to a 0.25 μm finish. The V barrier foil was 125 μm thick and was cut into 5 mm diameter disks. The V foil was ground down to a thickness of approximately 100 μm and polished through a 0.25 μm finish on both sides in air atmosphere. The Cr foil was purchased at 500 μm thickness and was cut into 5 mm diameter disks. The disk thickness was reduced to 100 μm. During thinning, it was determined that the Cr foil was brittle. In order to mitigate the Cr foil brittleness issues, a section of chromium foil was annealed in a vacuum furnace at 900 °C for 24 h under continuous argon flow (Ar purity of 99.999%). The annealed Cr barriers were used in all three diffusion couples with the as-received only incorporated in one diffusion couple. It should be noted that no microstructural characterization was performed on the fuel or the barriers prior to annealing tests, which includes understanding the oxide formation related to sample preparation.

Fig. 1 shows the diffusion couple layouts for the experimental tests, respectively. Sample preparation is consistent between both diffusion couples including Cr (Fig. 1a,b), V (Fig. 1a and b), and thermal annealed Cr (Fig. 1c and d). The sample preparation methods described here were incorporated for all diffusion couples. Note that the sections are not to scale. Sections were placed in contact with other materials in the layout. A Kovar steel jig was used based on its low thermal expansion properties and hand tightened to 12 in-lbs. Yttria (Y_2O_3) spray was used to coat the bolt threads and prevent galling of the steel. Tantalum foil was wrapped around the HT-9 ends of the diffusion couple to provide a more natural separation from the jig. Another tantalum foil was wrapped around the outside of the jig to help with gettering of any oxygen which may be present during the annealing of the samples in the furnace. The jig screws were torqued to 12 inch-pounds. The jig containing the diffusion couple was heated in a Carbolite model MTF10/25/130 furnace located in a continuous inert argon flow (Ar purity of 99.999%) atmosphere glovebox. Separate diffusion couples were heated to a temperature of 973 K (700 °C) for 100 h and 200 h. At the conclusion, the jig was cooled and disassembled.

After annealing, diffusion assemblies were quenched in water to preserve the phases formed upon heat treatment. The diffusion couple was removed from the compression device, mounted with the fuel cladding interface perpendicular to the analysis surface, and set in epoxy. Each couple was mounted in a 1" met-mount ring using long set epoxy and allowed to cure for more than 24 h. Samples were polished to plane with a final grit of 800 finish in an inert argon atmosphere. Scanning Electron Microscopy (SEM) met-mounts were loaded into an air glovebox and polished to a mirror finish of 0.25 μm for SEM and Focused Ion Beam (FIB) characterization.

2.2. SEM and FIB characterization

Diffusion couples were analyzed using JEOL-7000F SEM equipped with Energy Dispersive Spectroscopy (EDS) and confirmed by Wavelength Dispersive Spectroscopy (WDS). Secondary electron and backscatter electron imagining (SEI and BSE, respectively) were performed to show the underlying microstructure of the diffusion couple layers. EDS was performed in the form of line scans and X-

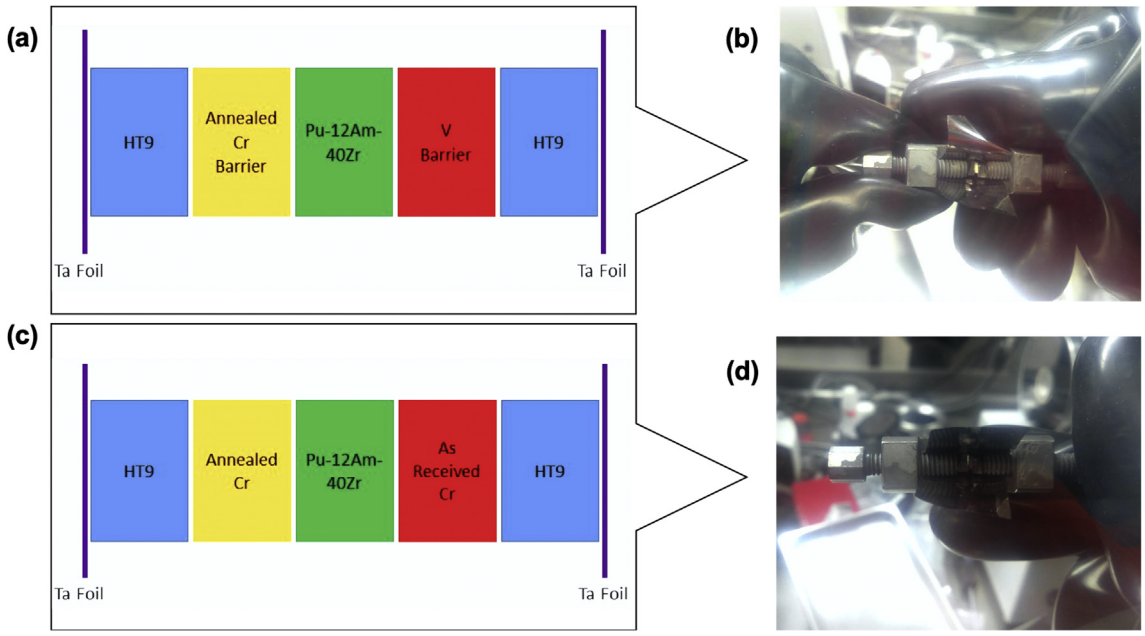

Fig. 1. (a) Starting with evaluating annealed Cr and V barriers a combined diffusion couple (b) was assembled inside an inert gas environment. (c) Evaluating the effect of annealing time a second diffusion was (d) similarly assembled.

ray maps to determine the chemical element distributions across the diffusion couples. In the EDS line scans and maps, each element was mapped using a specific electron shell signal. For example, the Zr map and line scan results were using the signal from the Kα1 peak. Similarly the Pu—*K*, O—*K*, Cr-*L*, and V-*L* peaks were utilized to generate these accompanying elemental maps.

FIB characterization was performed using an FEI Quanta 3D FIB. Cross-section imaging was performed to verify that the microstructure of the surface of the sample were consistent below the surface. Transmission Electron Microscopy (TEM) lamellae were lifted from the interfacial areas of interest in the diffusion couples. TEM lamellas had a nominal dimension of 15 μm × 10 μm × 0.1 μm.

2.3. Transmission electron microscopy characterization

Identification of formed phases was conducted utilizing high-resolution transmission electron microscopy imaging, spectroscopy, and selective area electron diffraction (SAED). Both a high-resolution JEOL 2010 and FEI Titan ChemiSTEM were utilized and operated at 200 kV to study electron transparent lamellae lifted from diffusion couples at each interface. The JEOL 2010 utilized a high tilt stage to collect SAED patterns on a gain referenced Gatan CCD camera. From these collected patterns, an azimuthal 2-dimensional integration was performed compared against simulated patterns from published crystal structures inside the Crystal Maker software to resolve lattice d-spacing and crystal structure. In addition, atomic lattice d-spacing of each diffraction pattern was measured and compared to published crystallographic data.

Using an FEI Titan ChemiSTEM equipped with four high solid angle 80 mm^2 windowless Si X-ray detectors was operated in high-resolution TEM and STEM modes. For STEM analysis, a sub-nanometer-sized probe was used to image the sample combining high annular dark field (HAADF) and bright field imaging and spectroscopy. In addition, HAADF imaging, both medium and annular bright field (ABF) images, were collected and stored. Energy dispersive X-ray spectral (EDS) mapping was operated in the same condition to acquire the Pu—*K*, Zr—*K*/*L*, O—*K*, Cr-*L*, and V-*L* with the best achievable spatial and energy resolution. Multiple spectral scans were performed with a nanometer analytical probe size and high beam current. Elemental quantification was performed inside the Bruker Scientific software utilizing a Cliff-Lorimer thin film TEM sample correction to process the EDS spectra and calculate weighted atomic maps [13]. Weighted spectral images were visualized inside the Bruker software that accounted for the specific atomic cross-sectional k-factors resulting in quantitative maps. These nominalized maps were compared against the accompanying HAADF image. The quantitative differences of particles, interfaces, voids, and layers were compared to assess the formation of additional phases and features tracking the annealing process.

3. Experimental results and discussion

The Pu—40Zr and Pu-12Am—40Zr diffusion couples with an annealed Cr and V barriers on opposite ends of the fuel sections held at 973 K (700 °C) for 100 h form our baseline to compare subsequent changes in solid-state chemistry and additional phase formation. As-annealed Cr in contact with Pu-12Am—40Zr was studied at 100 h and 200 h to study the effects of time at temperature on the resulting microstructures. As a single variable, time at temperature as received and annealed Cr barriers was held for the same 973 K (700 °C) for 200 h in contact with Pu-12Am-40Zr.

The analysis of the resulting interfaces and chemistries described reveals a complex and highly variable behavior that differs significantly from sample to sample. In this section, we compare and discuss the different morphologies observed in Pu—Zr based fuels with Cr and V barrier interfaces due to the effects of temperature and time as separate sections.

3.1. Effect of Am addition to the Pu—Zr based fuel in contact with an annealed Cr barrier

Diffusion couples 1, 2, and 3 compare the effects of Am addition to the fuel and its effects on the resulting diffusion layer between the fuel and the annealed Cr barrier. DC1 and DC2 were heat-treated at 700 °C for 100 h. In DC3, the sample was held at

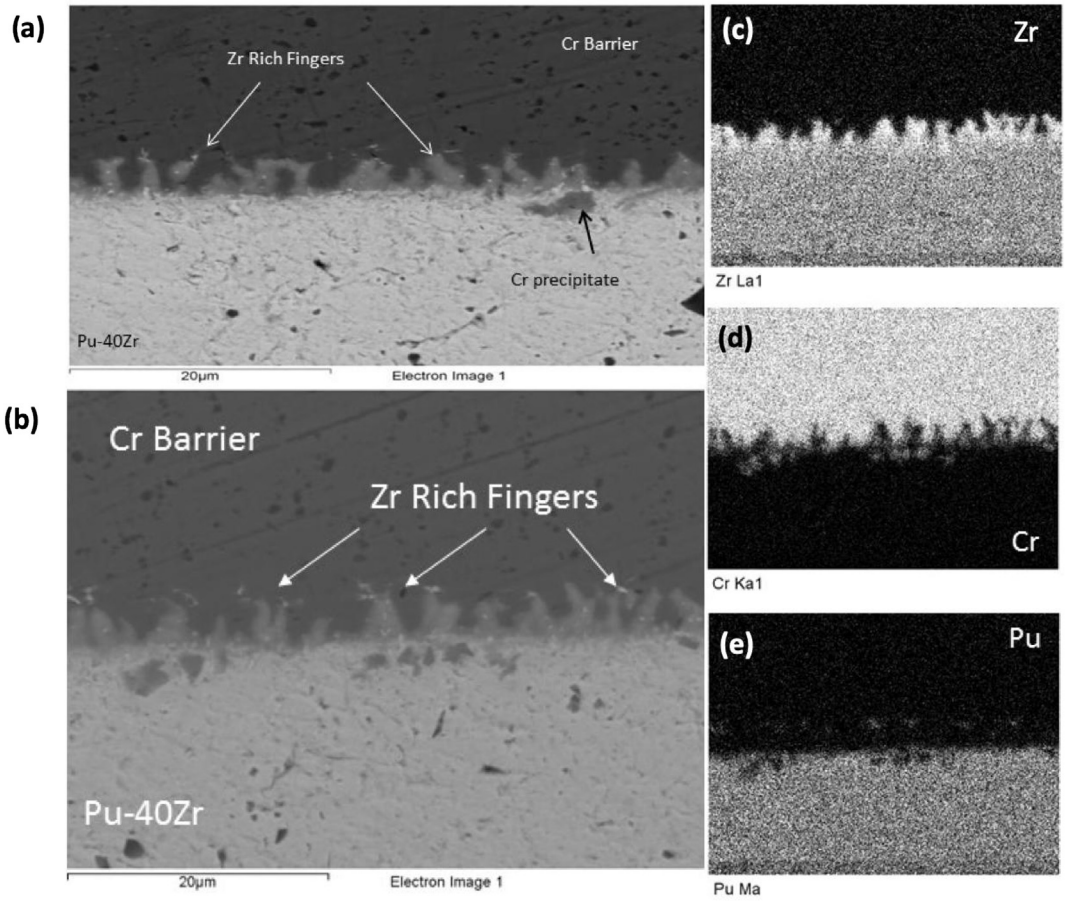

Fig. 2. (a) SEM micrograph of the general microstructure of Pu–40Zr vs. annealed Cr barrier and (b) EDS maps of the (c) Zr, (d) Cr, and (e) Pu distributions at the Pu–40Zr and annealed Cr barrier.

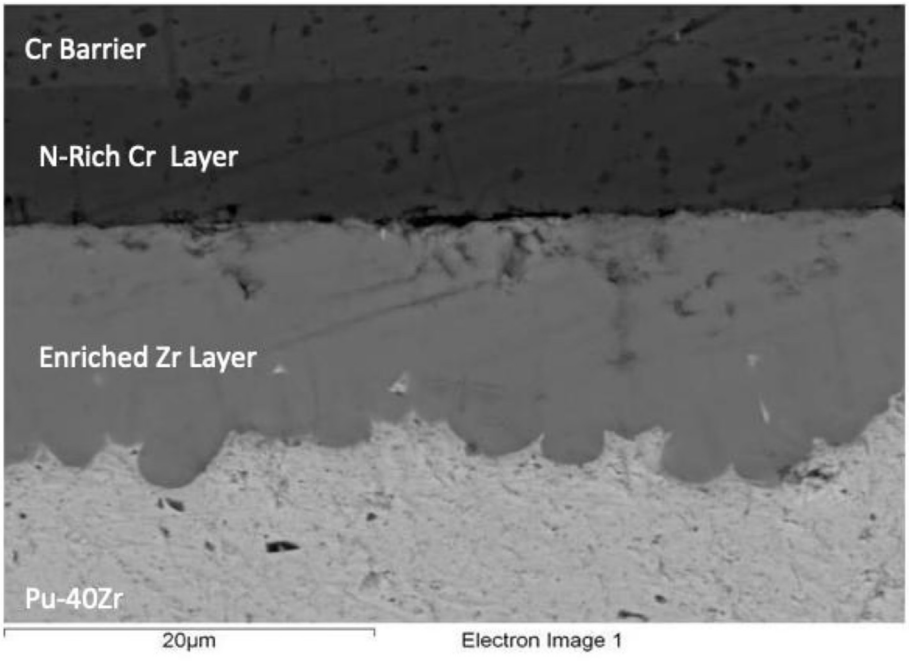

Fig. 3. Material chemistry and distribution of Pu–40Zr/annealed Cr for 100 h at 973 K (700 °C) in SEM plane view viewed in cross-section.

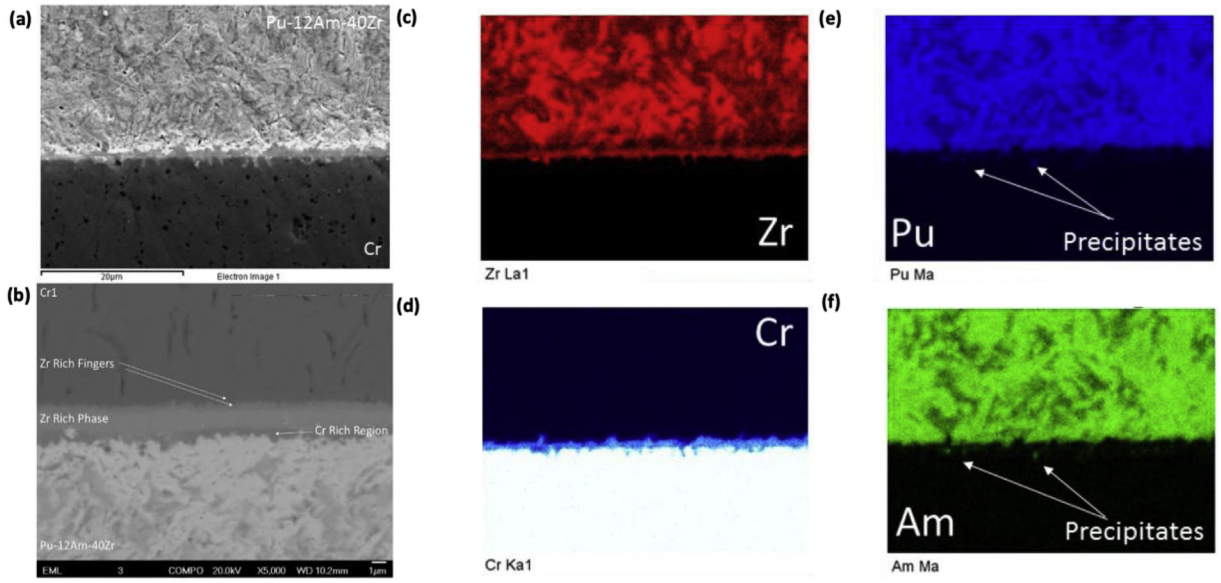

Fig. 4. Material chemistry and distribution of Pu-Am-Zr/annealed Cr for 100 h at 973 K (700 °C) viewed (a) plane view of the sample, (b) similarly viewed in cross-section, inside the SEM. X-ray based EDS chemical imaging on the cross section was performed to resolve the distribution of (c) Zr, (d) Cr, (e) Pu, and (f) Am. Units are reported in EDS net counts.

temperature for 200 h to see the effects of time at temperature for the annealed Cr barrier. The difference in time at temperature will be discussed in the later discussion section. In DC1, debonding was seen to occur between the Pu–40Zr fuel and the Cr barrier. This led to a reduced area of contact between the Pu–40Zr and Cr barrier. Fig. 2a shows the general microstructure of the Pu–40Zr in contact with the annealed Cr barrier while Fig. 2b shows an EDS map of the microstructure focusing on Zr (Fig. 2c), Cr (Fig. 2d), and Pu (Fig. 2e). Three features are seen to form after heat treatment. An interaction layer composed of Zr rich fingers is formed at the interface of the fuel and Zr barrier. Pu precipitates formed that are associated with the Zr rich fingers in the material. Randomly distributed Cr

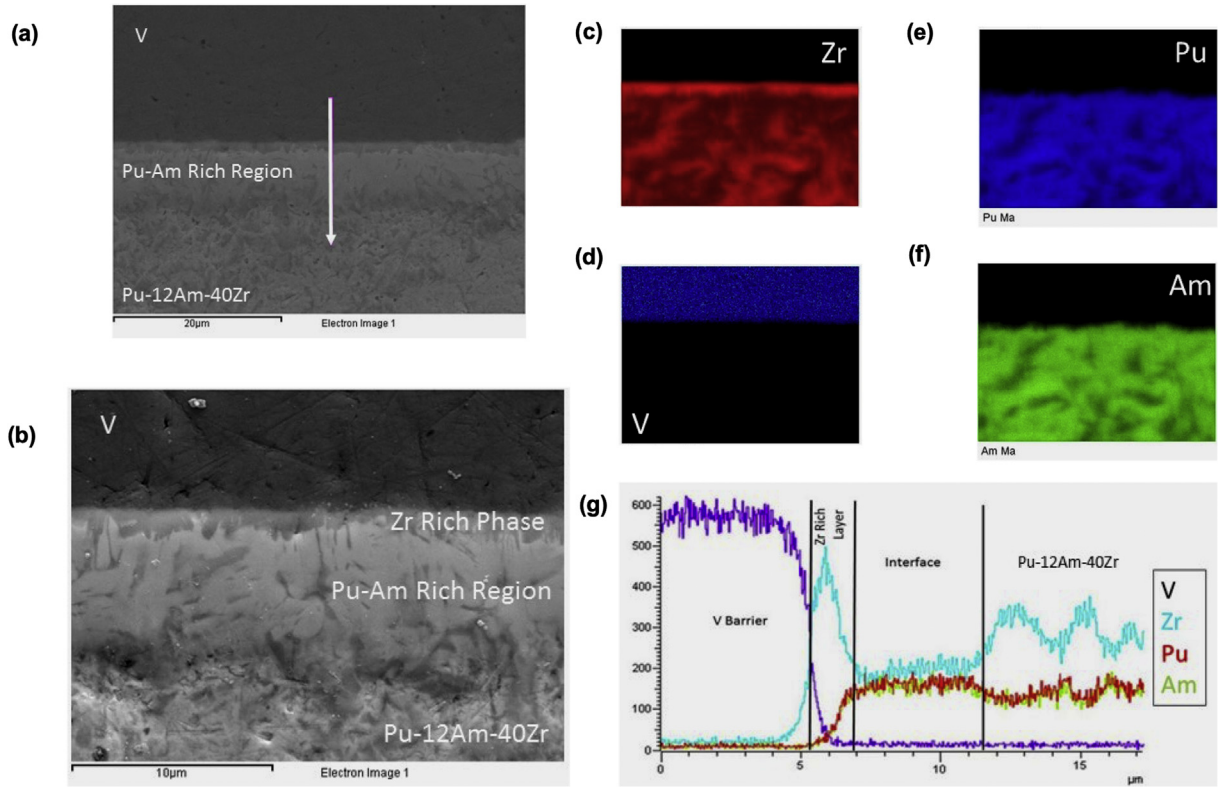

Fig. 5. Material chemistry and distribution of Pu-Am-Zr/V at 100 h viewed in (a) plane view and (b) cross-section inside the SEM. X-ray based EDS chemical imaging on the cross section was performed to resolve the distribution of (c) Zr, (d) V, (e) Pu, and (f) Am. (g) Based on chemical mapping an integrated profile transversing the multiple interfaces is reported. Units are reported in EDS net counts.

precipitates were seen to form on the fuel side of the interaction layer.

Fig. 3 shows the typical microstructure in the areas that were near the debonding of Pu–40Zr fuel and the Cr barrier in DC1. As identified by EDS measurements, there is an N-rich Cr layer that forms on the Cr barrier side of the interaction layer. This is a sampling artifact associated with the N_2 glovebox used during the heat treatments. This N-rich phase formed from insufficient contact between the fuel and the barriers during loading in the diffusion couple. Areas shown were in contact and void of the N-rich Cr layer. In addition to the N-rich Cr layer, an enriched Zr layer is formed on the fuel side of the interaction layer.

Fig. 4a reveals the chemical interaction between Pu-12Am–40Zr fuel and annealed Cr barrier, where there are distinctly three layers that have formed. These layers (cladding to fuel) are designated as the Zr rich fingers, an enriched Zr layer, and a Cr rich region. Fig. 4b shows a higher magnification micrograph of the distinct layers and the associated elemental maps of Zr (Fig. 4c), Cr (Fig. 4d), Pu

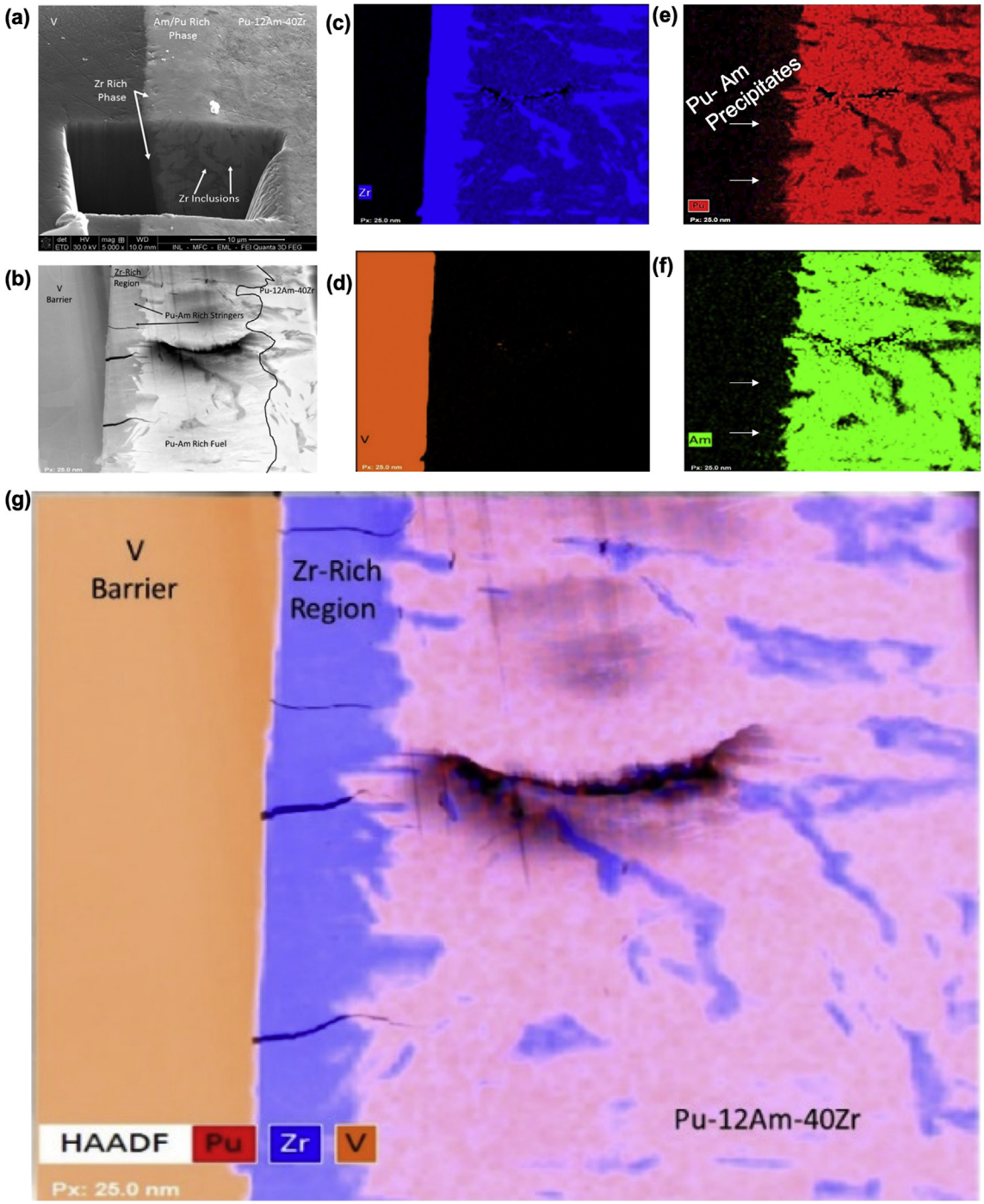

Fig. 6. Material chemistry and distribution of Pu-Am-Zr/V resolved with STEM atomic mass contrast imaging and EDS at 100 h. (a) Lifted from the sample is (b) electron transparent lamellae viewed in cross-section. X-ray based EDS chemical imaging on the cross section was performed to resolve the distribution of (c) Zr, (d) V, (e) Pu, and (f) Am. (g) Based on the chemical mapping, an 2-dimensional image on the chemical species of Pu, Am, and V is reported. Units are reported in EDS net counts.

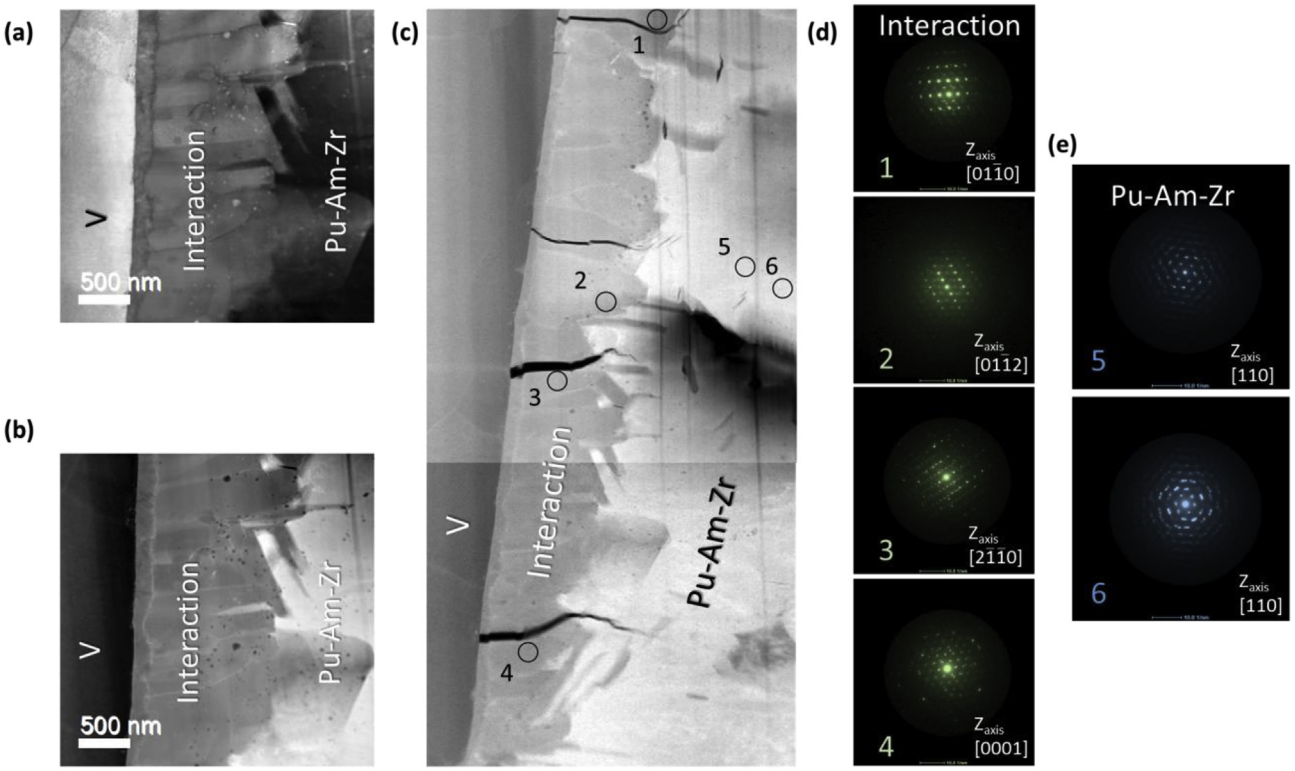

Fig. 7. The overall morphology and crystallographic structure of Pu-Am-Zr/V at 100 h were imaged with (a) bright field, (b) atomic mass contrast STEM and (c) at the specific points nanobeam diffraction patterns were collected and numbered. Each diffraction pattern numbered was indexed to known crystallographic phases. Well-oriented to different zone axes, the patterns resolve the structural transition from a hexagonal base interaction layer captured in (d) to the underlying e, cubic symmetry of the Pu-Am-Zr layer.

(Fig. 4e), and Am (Fig. 4f) at the same location. The chemical distribution confirms the suggested layering in the previous image, where between Pu-12Am–40Zr and annealed Cr, Cr-rich, and Zr-rich layers form after 100 h. The layers are further offset from one another, forming an additional interface and suggests there is diffusion between the two materials at 973 K (700 °C). In addition, resolved within the chemical maps, is the presence of Pu–Am precipitates and Zr-rich fingers extending into the Cr-barrier formed upon annealing. Randomly beyond the interaction layer on the fuel side we observed Zr precipitates (See Supplementary Figure 3). These features are indicative of additional effects to consider in the thermal annealing and chemical interaction between Pu-12Am–40Zr and Cr to be discussed in detail.

3.2. *Effect of Am addition to the Pu–Zr based fuel in contact with a V barrier*

As in the previous annealed Cr barrier discussion, diffusion couples 1 and 2 provide useful information on how Am addition to the U-free fuel affects the formation of diffusion layers between the fuel and V barriers. Following annealing amongst the V barrier interfaces, three microstructures form in Fig. 5a revealed by SEM. This includes the formation of a Pu–Am rich region, Zr-rich layers positioned between the Pu-12Am–40Zr and V barriers, and Pu–Am precipitates in the Zr-rich layer. Nearest the V barrier, a Zr-rich region formed that is similar to the region seen in the Cr-barrier sample in Fig. 5b, with nanocrystalline grains confirmed by TEM SAED patterns. EDS mapping reveals the elemental distribution of Zr (Fig. 5c), V (Fig. 5d), Pu (Fig. 5e), and Am (Fig. 5f). In conjunction with these maps, Fig. 5g is the integrated EDS chemical profile, revealing the concentration profile centered over the interaction region. For higher magnification studies, Fig. 6a reveals lifting at an electron transparent cross section from the Pu-12Am–40Zr/V diffusion couple. Within the STEM, Fig. 6b reveals the resulting microstructure, where the distribution for Zr (Fig. 6c), V (Fig. 6d), Pu (Fig. 6e), and Am (Fig. 6f) is imaged with higher magnification. Mapping the morphology for each of the elements, Fig. 6g shows the layer concentrations for Zr are lower compared to the fuel rich region.

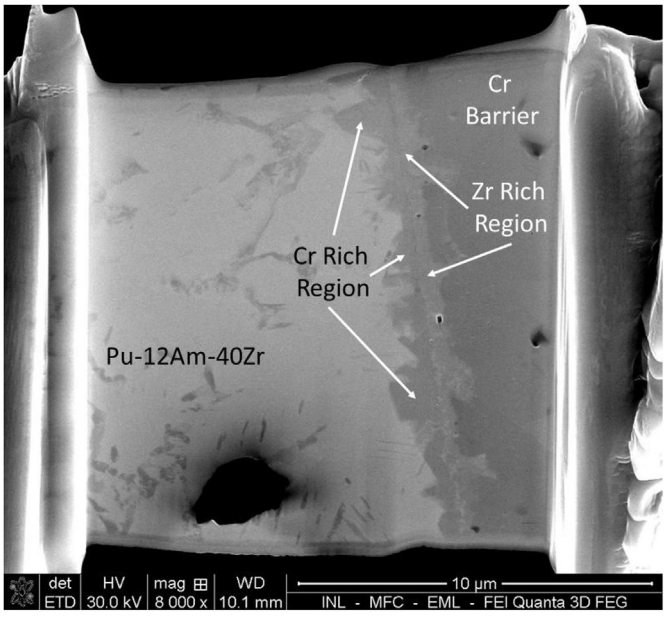

Fig. 8. FIB-SEM cross-section of Pu-Am-Zr/As-Annealed at 200 h anneal time.

Fig. 7a reveals the complex interaction layer, that formed intergranular grains at the interface between the fuel and cladding.. Fig. 7b in atomic contrast reveals Pu–Am precipitates within the interaction region, accompanied by multiple cracks. Imaging over the interaction region in detail Fig. 7c shows the interaction layer and morphology, where at specific points, nano-beam diffraction patterns were collected. The nano-beam diffraction patterns are reported in Fig. 7d for multiple orientations. Fig. 7e validates the crystallography of Pu-Am-Zr based on two selected area diffraction patterns far from the interaction region [14].

Nearest the Pu-Am-Zr fuel is a region described as a Pu–Am rich region. This region is the same as the base Pu-12Am–40Zr fuel with a lower density of Zr inclusions compared to further in the fuel. Free Zr present in the inclusions diffused to the barrier interface and formed the ZrO_2 phase, leaving a lower density of Zr inclusions and the appearance of a different microstructure compared to the base fuel. It should be noted that the Cr barrier diffusion couples form a similar region that is not as pronounced as the one reported in the V barrier samples.

3.3. Time effect on annealed Cr barrier in contact with Pu-12Am–40Zr fuel

Another aspect of the study was to understand the kinetics of the diffusion layer growth with increasing annealing time. One portion of diffusion couple 3 was focused on the effects of annealing time up to 200 h. This can be compared to DC2 where the same fuel and cladding was annealed to 100 h. Fig. 8 shows the typical microstructure of the Pu-12Am–40Zr/as-annealed Cr barrier interface at 200 h anneal time. Thickness measurements of both the 100 and 200 h diffusion couples were performed and found to be 1.55 ± 0.56 μm and 2.08 ± 0.37 μm. Analysis of the diffusion kinetics and formation free energies will be further reviewed in the discussion portion of this paper.

The increased thickness of the diffusion layer in DC3 allowed was selected to understand the phases created during the annealing process. Fig. 9 revealed the chemical interaction between Pu-12Am–40Zr and annealed Cr for 200 h as a baseline. Fig. 9a reveals the specimen was lifted out from the interface with site-specific FIB and studied in cross-section. Fig. 9b in cross-section reveals four distinct layers, including the Cr barrier, followed by two distinct intercalation layers formed after interacting with Pu-12Am–40Zr for the 200 h of annealing at 973 K (700 °C). EDS spot checks in the SEM reveals these two interface layers differ in the amount of Cr and Zr present, identified in Fig. 9b as Cr and Zr-rich. Given the need for higher resolution, the cross-section was thinned to electron transparency and studied inside an FEI Titan ChemiSTEM. Fig. 9c is the atomic contrast image that reveals the same layering (Pu-12Am–40Zr/Cr-rich layer/Zr-rich layer/Cr), but with additional features in these layers, including precipitates and a well-defined interface between the two layers. Bright field STEM Fig. 9d reveals these same features, with the additional confirmation for the presence of He bubbles (See Supplementary Information Figs. 1 and 2) and bright voids that form within the Cr barrier [15]. This specimen establishes the baseline chemical and physical behavior associated with the interaction between these alloys and Cr.

3.4. Effects of Cr processing in contact with Pu-12Am–40Zr at 973 K (700 °C)

While testing the effects on the microstructure at 973 K (700 °C)

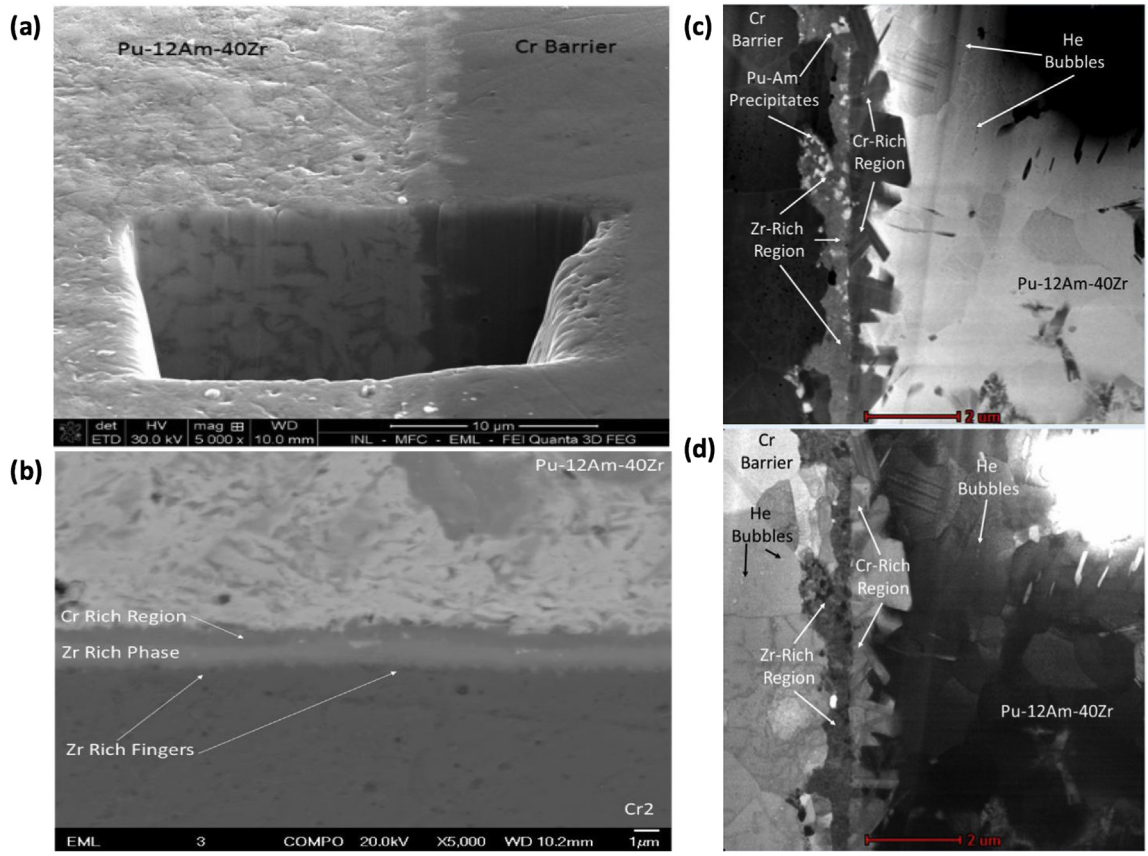

Fig. 9. Material distribution of 200 h anneal for Pu-12Am–40Zr with as-received Cr at 973 K (700 °C) (a) sample viewed from the surface, (b) in cross section and imaged with (c) atomic mass contrast and (d) bright field STEM.

for an extended thermal annealing time of 200 h, DC3 was studied to see the effects on the processing of the Cr barrier adjacent to the fuel. The as-received Cr barrier was tested with the annealed Cr barrier to see if any difference in the microstructure occurs. Fig. 10a provides an overview micrograph of the diffusion zone between Pu-12Am–40Zr and the as-received Cr barrier. Cracking was seen in the foil, indicating the brittleness of the barrier. Comparatively, Fig. 10b is the as-received Cr and Fig. 10b is the annealed Cr diffusion couple. Microstructurally, there are no visible differences between the two Cr barriers indicating while at temperature, the same diffusion mechanisms are prevalent.

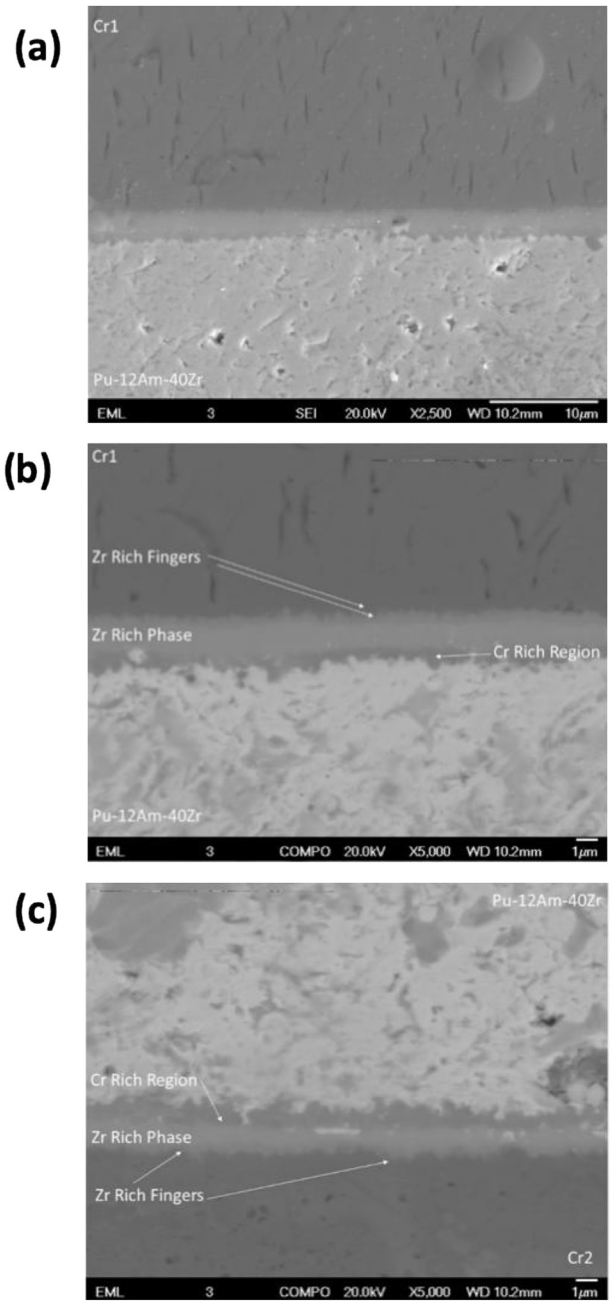

Fig. 10. (a) General overall microstructure of the as-received Cr barrier/fuel interface in DC3 and comparison of the diffusion layers in DC3 for (b) as-received Cr and (c) annealed Cr.

4. Discussion

4.1. Cr barrier effects

As seen in Fig. 2, there are two distinct layers that have formed due to the thermal annealing process. Prior to understanding how these layers form, some generalizations about the starting microstructure of the fuel and the Cr barriers is inferred. Both of these materials were prepared in an air atmosphere, leading to the formation of oxide layers on the surface. Microstructural characterization was not performed on these materials prior to thermal annealing process that showed pure Cr samples exposed to air at elevated temperatures, form a passive oxide layer composed of Cr_2O_3 on the surface. The Cr_2O_3 phase is one of the starting basis for phases observed in annealing studies. It is unclear how the Cr barrier was formed at Alfa Aesar and if any heat treatments were performed on the foil prior to purchasing. This can be true of the V barrier, as well. While a certificate of analysis can provide some purity of the feedstock, it is unclear where any of the impurities, such as O, reside in the foil.

The fuels, both Pu–40Zr and Pu-12Am–40Zr, likely form a Zr rich passive layer at the surface of the fuel, which was shown in Fig. 3 and is suggested by Janney et al. as the starting point for Zr-rich inclusions in actinide Zr alloys is oxygen, nitrogen, or carbon impurities [8,16]. The formation of nano-sized ZrO_2 crystals allows for other Zr to accumulate and eventually stabilize the formation of α-Zr. These are the Zr inclusions seen in the interior fuel region of the fuel. The inclusions that are near the polished surface of the sample will readily form oxides with the exposed air, forming ZrO_2. Fig. 11 shows a cartoon of the formation of the different layers at the diffusion barrier and fuel interfaces for the V and Cr barriers. This includes starting material conditions, assembly of the diffusion couple, and the results of the annealing process. This illustration will be used extensively during the discussion of the results. Fig. 11a illustrates the starting configuration for the fuel and the Cr barrier with the natural surface oxide layer that forms following exposure to air. These layers were in contact with each other when the diffusion couples were assembled, as shown in Fig. 11b.

After thermal annealing studies, three phases/features formed at the interface. These being the Cr/Zr rich phase near the fuel region and near the Cr barrier, Zr-rich finger features, and Pu/Am rich precipitates. To explain why each of these features form, Gibbs free energy of anticipated phases was researched. To help understand the formation of the Zr-rich fingers extending into the Cr barrier, it is important to understand the free energies for Zr, Cr, and their oxides. Gibb free energy values for Zr/ZrO_2 and Cr/Cr_2O_3 are −950 and −600 kJ/mol O_2 at 700 °C, respectively [17,18]. This indicates that any free oxygen or oxygen tied to the passive Cr_2O_3 layer from oxidation in air will be consumed by Zr readily at temperature. As seen in the Zr-rich finger regions, the fingers only form in the first few microns of the Cr barrier, where likely the passive oxide Cr_2O_3 layer formed on the surface of the Cr barrier during sample preparation. This process is expected to continue until any remaining oxygen is consumed or all free Zr metal is consumed. The microstructure of the Zr-rich fingers shows that they are forming along grain boundaries in the Cr barrier. This is expected as O_2 will have increased diffusion kinetics on grain boundaries compared to the bulk, forming Cr_2O_3 more readily and only in the bulk adjacent to the surface exposed to air..

The consumption of the Cr_2O_3 layer will leave excess free Cr metal at the interface. This excess Cr metal will seek a low energy state. From the Cr–Zr phase diagram [19], two phases should form at the annealing temperature, α-Zr, and $ZrCr_2$. It is likely that these two phases compose the Cr-rich region that was pointed out in Figs. 2 and 11d. EDS measurements in the Cr region show atomic

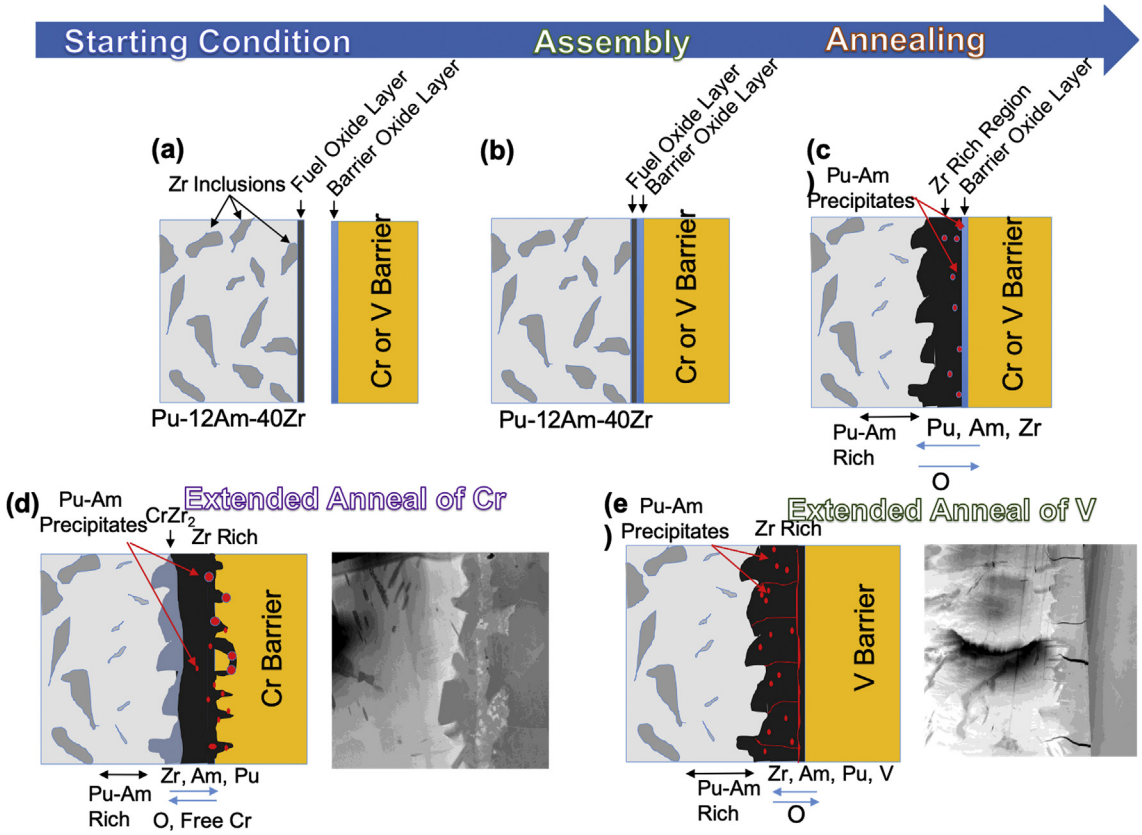

Fig. 11. Schematic summary comparing the observed chemical morphologies at the Pu-Am-Zr-Cr/V interface starting with (a) separate components and (b) assembly evolving as a consequence of (c) annealing, and consumption (d) Cr and (e) V barriers.

concentrations of ~40% Zr and ~60% Cr. These results are close to the anticipated 33% Zr and 66% Cr value for $CrZr_2$. It is likely that some α-Zr is present in the region, skewing the results slightly and leading to slightly higher Zr content. TEM diffraction characterization was not performed in this region to provide confirmation of the $ZrCr_2$ phase.

The other feature seen in the interface region was Pu–Am rich precipitates. These precipitates are located mostly in the Zr-rich finger regions and towards the Cr barrier, indicating that they have a high affinity of oxygen. The Pu–O phase diagram at 700 °C shows that the three phases can be present, PuO_{2-x}, Pu_2O_3, and $PuO_{1.61}$ [20]. Pu_2O_3 and $PuO_{1.61}$ have higher Gibbs free energies than ZrO_2. PuO_2 has a similar energy to ZrO_2 [21]. The Am oxygen potential is higher than ZrO_2 and will readily form oxides preferentially compared to ZrO_2. High-resolution TEM measurements were not performed on these Pu–Am precipitates to determine the phase of these precipitates. It is hypothesized that the oxygen content present will dictate that an oxygen deficient environment will be present and lead to the formation of oxides with lower oxygen content such as Pu_2O_3 and $PuO_{1.61}$ as compared to PuO_2 supported in part by the work of Guéneau et al. [22]. This is a potential reason for the formation of these phases found at the end of the Zr fingers closest to the Cr barrier as they have the highest affinity of oxygen.

4.2. V barrier effects

Comparing to the V barrier, Fig. 11e highlights there is no additional interaction in general, reported in Fig. 5a and b and chemically resolved in Fig. 5c–e, resulting in the growth of an oxide riddled with Pu–Am precipitates within the interaction layer imaged in Fig. 6a and b and chemically resolved in Fig. 6c–f with STEM-based EDS profiling. The Pu–Am precipitates likely form given the oxygen-deficient environment, where if more oxygen were present Pu_2O_3 and $PuO_{1.61}$ should form as previously noted by Miller and Reimann [23]. In this case, the self-limiting oxide growth further results in cracking with V, due potentially to the mechanical stress and differences in thermal expansion associated with additional oxide growth, further constrained by the lattice mismatch of Pu-Am-Zr and V, identified in Fig. 7a–c as a hexagonal to a cubic mismatch between the interaction layer and fuel rich region, respectively. The interaction layer in Fig. 7d constitutes a polycrystalline morphology with multiple orientations, all classified to the hexagonal space group P63/mmc, with lattice parameters $a = b = 3.2392$ Å, $c = 5.1722$ Å, $\alpha = 90°$, $\beta = 90°$, and $\gamma = 120°$. In the fuel rich region, the structure identifies as a rock-salt cubic structure with a lattice parameter $a = b = c = 4.78848$ Å, and $\alpha = \beta = \gamma = 90°$.

The third microstructure seen in the V barrier/Pu-based fuel specimens was a Pu–Am rich precipitates forming between the Zr-rich region and the base Pu-12Am–40Zr alloy. This is similar to the same effects as discussed in the Cr barrier section, where the Gibbs free energy of formation of V_2O_3 at 700 °C (~–650 k/mol O_2) is less than Pu_2O_3 and $PuO_{1.61}$. This leads to the reduction of the V oxide and preferential formation of the Pu–Am oxides. In excess, we suspect the V free metal forms a passive oxide layer, that remains at a low enough concentration in the bulk, that we could not observe using EDS.

Comparing the barriers, since there is a significant difference in the thermal expansion coefficients that leads to cracking in V, there is a preference for a Cr barrier [24]. Once the Cr_2O_3 forms the layer is stable and does not lead to additional changes in morphology.

The observation of cracking with V limits the engineering applicability of this barrier for nuclear applications.With a Cr barrier, there is also excess Cr metal that seeks a low energy state, preferentially as an oxide, which suggests there is an additional benefit to a Cr over V barrier.

5. Concluding remarks

SEM and analytical TEM were used to identify the phases formed between U-free Pu-Am-Zr fuels and V/Cr barriers at elevated temperatures. This includes testing different Cr processed barriers and time at temperature. Comparing the 100 h and 200-h tests for the interaction between Pu-12Am−40Zr fuel and Cr suggests a weakening in the interfacial growth rate as a function annealing time. This is indicative of a diminishing oxygen concentration in the Cr and V barriers.. In the Cr barrier diffusion couples, distinct phases formed following annealing, including Pu−Am precipitates near the Cr barrier and a ZrO_2 phase near the Cr barrier interface. ZrO_2 and Pu−Am precipitates phases form oxides from the existing Cr_2O_3 passive surface oxide layer formed on the Cr barrier during sample preparation. The free Cr metal from the pre-existing Cr_2O_3 layer later diffuses towards the fuel and interacts with free Zr in the fuel to form $CrZr_2$ precipitate phases. In the V barrier, two of the phases seen in the Cr barrier diffusion couples formed, the ZrO_2 and Pu−Am precipitates. Formation of these oxide phases is energetically favorable compared to staying in the V_2O_3 phase present on the surface of the V barrier.. While these diffusion couple experiments were focused on a single temperature with other varying parameters, the Cr and V barriers were useful in minimizing the formation of a diffusion layer (<3 μm thickness) between the barriers and the U-free Pu based Zr fuels.

6. U.S. Department of Energy disclaimer

The U.S. Government retains a nonexclusive, royalty-free license to publish or reproduce the published form of this contribution or allow others to do so, for U.S. Government purposes. This information was prepared as an account of work sponsored by an agency of the U.S. Government. Neither the U.S. Government nor any agency thereof, nor any of their employees, makes any warranty, express or implied, or assumes any legal liability or responsibility for the accuracy, completeness, or usefulness of any information, apparatus, product, or process disclosed, or represents that is use would not infringe privately owned rights. References herein to any specific commercial product, process, or service by trade name, trademark, manufacturer, or otherwise, does not necessarily constitute or imply its endorsement, recommendation, or favoring by the U.S. Government or any agency thereof. The views and opinions of authors expressed herein do not necessarily state or reflect those of the U.S. Government or any agency thereof.

Acknowledgments

The authors acknowledge support by the Ministry of Education, Culture, Sports, Science and Technology of Japan (MEXT) through Toshiba Energy Systems and Solutions Corporation in the framework of MEXT's Nuclear System Research and Development Program. JAA acknowledges work supported in part through the INL Laboratory Directed Research & Development (LDRD) Program under DOE Idaho Operations Office Contract DE-AC07-05ID145142 and the Office of Nuclear Energy under the Department of Energy. Authors also acknowledge Doug Porter, Seongtae Kwon, Jian Gan, and Sebastien Teyessyre for helpful discussions and suggested edits.

Appendix A. Supplementary data

Supplementary data to this article can be found online at https://doi.org/10.1016/j.jallcom.2019.152735

References

[1] D.E. Burkes, R.S. Fielding, D.L. Porter, Metallic fast reactor fuel fabrication for the global nuclear energy partnership, J. Nucl. Mater. 392 (2009) 158−163, https://doi.org/10.1016/j.jnucmat.2009.03.009.
[2] C.L. Trybus, J.E. Sanecki, S.P. Henslee, Casting of metallic fuel containing minor actinide additions, J. Nucl. Mater. 204 (1993) 50−55, https://doi.org/10.1016/0022-3115(93)90198-8.
[3] L.H. Hamilton, B. Cowcroft, M.H. Ayers, V.A. Bailey, A. Carnesale, P.V. Domenici, S. Eisenhower, C. Hagel, J. Lash, A.M. Macfarlane, R.A. Meserve, E.J. Moniz, P.F. Peterson, J.W. Rowe, P. Sharp, Blue Ribbon Commission on America's Nuclear Future: Report to the Secretary of Energy, Blue Ribbon Commission on Americas Nuclear Future, BRC), 2012.
[4] Y. Arita, Y. Tsuboi, H. Ohta, Innovative TRU Burning Fast Reactor Cycle Using Uranium-free TRU Metal Fuel - (2) Fundamental Properties of Uranium-free TRU-Zr Metal Fuel - 5093, GLOBAL 2015 Proceedings, 2015. http://inis.iaea.org/Search/search.aspx?orig_q=RN:49023720. (Accessed 31 May 2019).
[5] W.J. Carmack, D.L. Porter, Y.I. Chang, S.L. Hayes, M.K. Meyer, D.E. Burkes, C.B. Lee, T. Mizuno, F. Delage, J. Somers, Metallic fuels for advanced reactors, J. Nucl. Mater. 392 (2009) 139−150, https://doi.org/10.1016/j.jnucmat.2009.03.007.
[6] M. Haas, J.D. Cerchione, R.J. Dunworth, R.M. Fryer, C.W. Wilkes, M.H. Derbidge, Fabrication of Driver-Fuel Elements for EBR-II, Argonne National Lab., IL (United States), 1979, https://doi.org/10.2172/711046.
[7] A. Aitkaliyeva, J.W. Madden, B.D. Miller, C.A. Papesch, J.I. Cole, TEM examination of phases formed between U−Pu−Zr fuel and Fe, J. Nucl. Mater. 467 (2015) 717−723, https://doi.org/10.1016/j.jnucmat.2015.10.043.
[8] D.E. Janney, J.R. Kennedy, J.W. Madden, T.P. O'Holleran, Crystal structure of high-Zr inclusions in an alloy containing U, Pu, Np, Am, Zr and rare-earth elements, J. Nucl. Mater. 448 (2014) 109−112, https://doi.org/10.1016/j.jnucmat.2014.01.044.
[9] C.E. Lahm, J.F. Koenig, R.G. Pahl, D.L. Porter, D.C. Crawford, Experience with advanced driver fuels in EBR-II, J. Nucl. Mater. 204 (1993) 119−123, https://doi.org/10.1016/0022-3115(93)90207-F.
[10] C. Matthews, C. Unal, J. Galloway, D.D.K. Jr, S.L. Hayes, Fuel-cladding chemical interaction in U-Pu-Zr metallic fuels: a critical review, Nucl. Technol. 198 (2017) 231−259, https://doi.org/10.1080/00295450.2017.1323535.
[11] K. Ishii, M. Yamaoka, Y. Moriki, T. Oomori, Y. Tsuboi, K. Arie, M. Kawashima, Development of uranium-free TRU metallic fuel fast reactor core, in: K. Nakajima (Ed.), Nuclear Back-End and Transmutation Technology for Waste Disposal: beyond the Fukushima Accident, Springer Japan, Tokyo, 2015, pp. 155−167, https://doi.org/10.1007/978-4-431-55111-9_15.
[12] Y. Tsuboi, K. Arie, C.A. Papesch, B.D. Miller, R.D. Mariani, Y. Arita, H. Ohta, Fundamental Properties for Evaluation of Uranium-free TRU-Zr Metal Fuel Performance, NV US, Las Vegas, 2016.
[13] M. Watanabe, D.B. Williams, The quantitative analysis of thin specimens: a review of progress from the Cliff-Lorimer to the new ζ-factor methods, J. Microsc. 221 (2006) 89−109, https://doi.org/10.1111/j.1365-2818.2006.01549.x.
[14] S. Grandjean, B. Arab-Chapelet, A.C. Robisson, F. Abraham, Ph Martin, J.-Ph Dancausse, N. Herlet, C. Léorier, Structure of mixed U(IV)−An(III) precursors synthesized by co-conversion methods (where An=Pu, Am or Cm), J. Nucl. Mater. 385 (2009) 204−207, https://doi.org/10.1016/j.jnucmat.2008.10.039.
[15] J.R. Jeffries, M.A. Wall, K.T. Moore, A.J. Schwartz, He bubble coarsening by migration and coalescence in annealed Pu−Ga alloys, J. Nucl. Mater. 410 (2011) 84−88, https://doi.org/10.1016/j.jnucmat.2011.01.015.
[16] D.E. Janney, J.R. Kennedy, As-cast microstructures in U−Pu−Zr alloy fuel pins with 5−8wt.% minor actinides and 0−1.5wt% rare-earth elements, Mater. Char. 61 (2010) 1194−1202, https://doi.org/10.1016/j.matchar.2010.07.012.
[17] R. Arroyave, L. Kaufman, T.W. Eagar, Thermodynamic modeling of the Zr-O system, Calphad 26 (2002) 95−118, https://doi.org/10.1016/S0364-5916(02)00027-5.
[18] A. Holzheid, H. St, C. O'Neill, The Cr-Cr2O3 oxygen buffer and the free energy of formation of Cr2O3 from high-temperature electrochemical measurements, Geochem. Cosmochim. Acta 59 (1995) 475−479, https://doi.org/10.1016/0016-7037(94)00287-V.
[19] B. Predel, Cr-Zr (Chromium-Zirconium), in: O. Madelung (Ed.), Cr-Cs − Cu-Zr, Springer Berlin Heidelberg, Berlin, Heidelberg, 1994, pp. 1−3, https://doi.org/10.1007/10086090_1030.
[20] Study of phase equilibrium of Pu2O3-PuO2 system by the first-principles calculation and CALPHAD approach - IOPscience (n.d.), https://iopscience.iop.org/article/10.1088/1757-899X/9/1/012035. (Accessed 31 May 2019).
[21] C.A. Beard, H.T. Blair, J.J. Buksa, D.P. Butt, K. Chidester, S.L. Eaton, T.J. Farish, R.J. Hanrahan, K.B. Ramsey, Nuclear Fuels Technologies Fiscal Year 1996 Research and Development Test Results, 1996, https://doi.org/10.2172/464372.
[22] C. Guéneau, C. Chatillon, B. Sundman, Thermodynamic modelling of the

plutonium–oxygen system, J. Nucl. Mater. 378 (2008) 257–272, https://doi.org/10.1016/j.jnucmat.2008.06.013.
[23] R.L. Miller, G.A. Reimann, Thermodynamics of Gas-Metal-Slag Equilibria for Applications in in Situ and Ex Situ Vitrification Melts, 1993. United States, http://inis.iaea.org/search/search.aspx?orig_q=RN:25003593.
[24] B. Ravat, L. Jolly, B. Oudot, A. Fabas, H. Guerault, I. Popa, F. Delaunay, New insight into δ-Pu alloy oxidation kinetics highlighted by using in-situ X-ray diffraction coupled with an original Rietveld refinement method, Corros. Sci. 138 (2018) 66–74, https://doi.org/10.1016/j.corsci.2018.03.046.